Project: **1021**
Project title: **Paleo-Constraints on Monsoon Evolution and Dynamics (PACMEDY)**
Principal investigators: **Johann Jungclaus (MPI-M), Eduardo Zorita (HZG), Gerrit Lohmann (AWI)**
Report period: **2019-01-01 to now**

Project overview

Monsoon systems influence the water supply and livelihoods of over half of the world. Past climates provide an opportunity to link recent and future changes and to improve understanding of mechanisms and predictability of monsoon variability. This project uses palaeoenvironmental records of climate variability and simulations with Earth System Models over the past 6000 years and investigate the Indian, Africa and South American monsoon systems, to provide a better understanding of their dynamics and interannual to multidecadal variability (IM). The simulations contribute to the Paleo Model Intercomparison Project (Kageyama et al., 2016) as part of the 6 th phase of the WCRP Coupled Model Intercomparison Project (CMIP6, Eyring et al., 2016).

Work accomplished by AWI-ESM

With the use of AWI-ESM2, we have conducted a transient experiment from mid-Holocene to

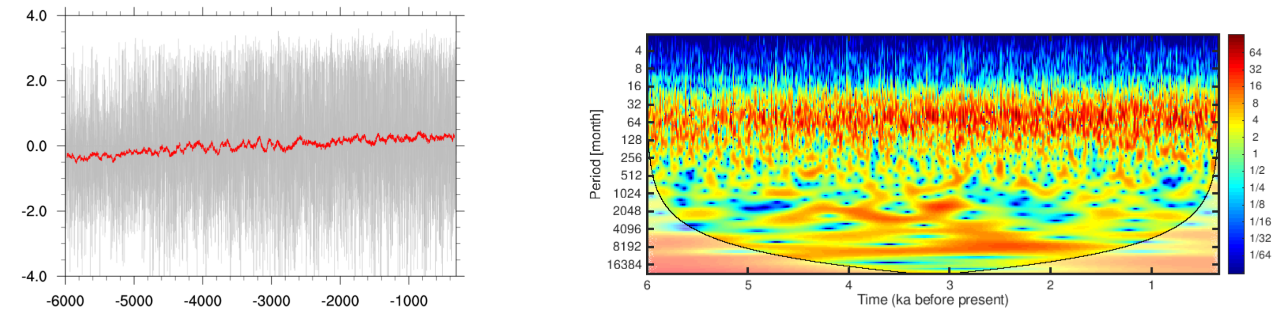

present, the ocean component uses a resolution of up to 30 km over polar regions and along coastal lines, and as coarse as 220 km over the far-field ocean, and the atmospheric grid is T31.
Fig. 1 (Left) Time series of NINO3.4 index. Gray line represents the raw data and the red represents the smoothed NINO3.4. (Right) Wavelet of NINO3.4 index.

We calculated the NINO3.4 index based on the average sea surface temperature anomaly in the region bounded by 5°N to 5°S, from 170°W to 120°W. Fig. 1 shows an increasing sea surface temperature over the NINO3.4 region and an increasing NINO3.4 variability. The period of the ENSO is as well enhanced from 6k to present.

Changes in the monsoon extent and strength are assessed using the following metrics: The monsoon extent is the land-only area where annual precipitation range, defined as the difference between summer and winter rainfall, exceeds 2 mm/day for each monsoon domain. The selected threshold warrants a concentrated summer rainy season and distinguishes monsoons from year-round rainy regimes. The monsoon strength is the average summer rainfall calculated in each monsoon domain:

1. Asian monsoon (5–23.3N, 60–120E).
2. African monsoon (5–23.3N, 20W-40E).
3. North American monsoon (0–30N, 120–40W).

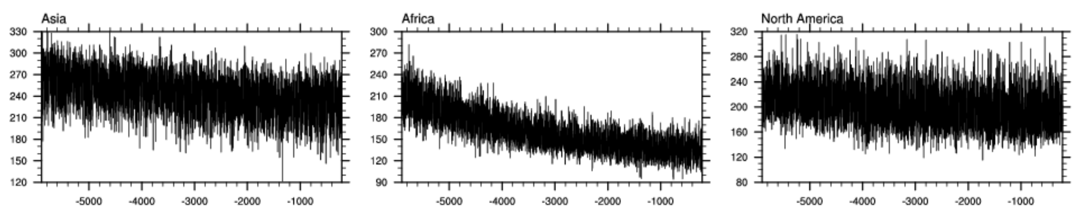

Fig. 2 Evolution of monsoon precipitations for each monsoon domain. (mm/month)

The evolution of monsoon precipitation for each domain is shown in Fig. 2. The Asia and Africa monsoon experience a reduced monsoon rainfall from mid-Holocene to present, with the most pronounced trends being before 4k, after 4k the reducing speed is getting smaller. For North America, there is a general decrease from 6k to 4k, then following by no significant changes in monsoon rainfall.

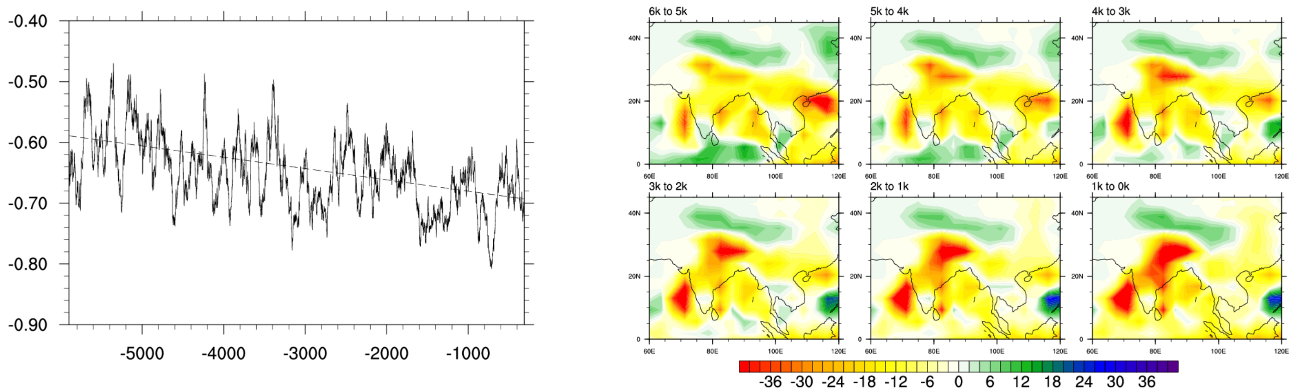

Fig. 3 (Left) Sliding correlation between NINO3.4 and Asian monsoon rainfall. (Right) Composite map of Asian summer rainfall anomalies during El Niño years for each millennium, trends are removed for all data.

Fig. 3 show a negative correlation of ENSO with the Asian summer monsoon. A 100-year sliding correlation index indicate an increasing effect of ENSO on the Asian summer rainfall, being 0.6 to 0.7 from mid-Holocene to present. In general, El Niño years (defined by NINO3.4 index being larger than 0.5 K) are associated with drier conditions over the South Asia, especially the Indian. Such relationship magnify itself from 6k to present. The enhanced correlation might lie on the increased NINO3.4 variability.

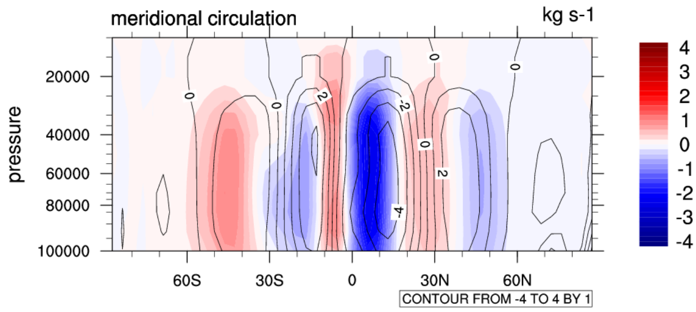

Fig . 4. DJF Zonal mean mass streamfunction (1 x10^9 kg/s) for (a) El Niño–La Niña composite. Contours are the climatological mean streamfunction.

Contrasting the zonal mean mass streamfunction (Fig. 4) of El Niño versus La Niña during the peak season (DJF months), the Hadley cells in both hemispheres tend to intensify and contract equatorward in the tropics, and the Ferrell cells move equatorward as well, especially in the SH. This is in agreement with the well-known Hadley Cell-ENSO relationship.

‘

Work accomplished by MPI-ESM:

The newly developed isotope-enhanced version of MPI-ESM, called hereafter MPI-ESM-wiso is used to simulated the mid-Holocene climate.

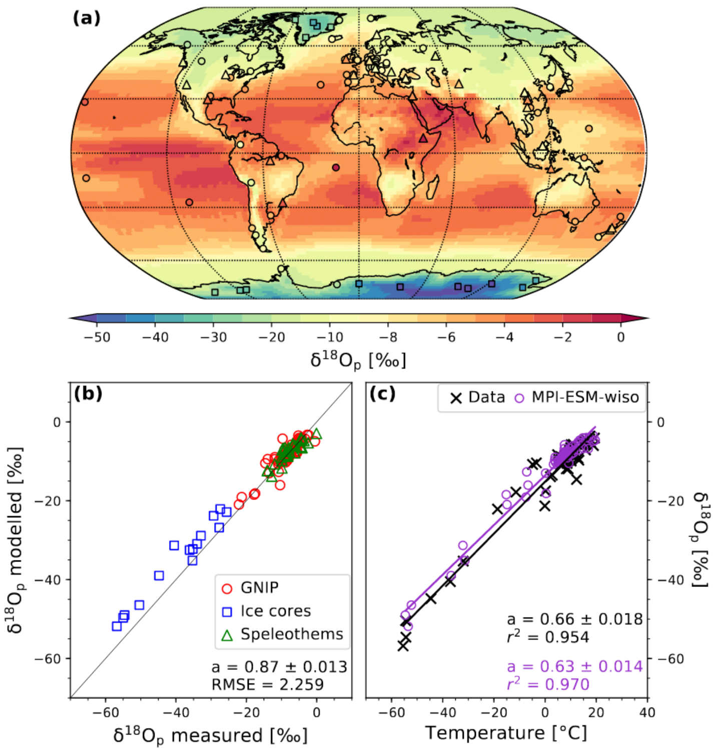

Fig. 5 (a) Global distribution of simulated (background pattern) and observed (colored markers, see text for details) annual mean $\delta^{18}O_p$ values in precipitation under pre-industrial conditions. (b) Modelled vs. observed annual mean $\delta^{18}O_p$ at the different GNIP, speleothem, and ice core sites.(c) Observed (black crosses) and modelled (purple circles) spatial $\delta^{18}O_p$–T relationship.

Fig. 5 shows the global distribution of the simulated annual mean $\delta^{18}O_p$ values in precipitation. The main well-known patterns of the global $\delta^{18}O_p$ distribution can be found in the model. They are very similar to those already observed with ECHAM5/MPIOM (Werner et al., 2016) and in agreement with the present-day observations (circles: GNIP, squares: ice cores, triangles: speleothems). Typically, enhanced depletion of $\delta^{18}O_p$ with decreasing temperature (temperature effect) and increased altitude (altitude effect) is well simulated by MPI-ESM-wiso. The lowest simulated values of $\delta^{18}O_p$ occur over the polar regions, with the most depleted value over East Antarctica (−54.5 ‰). Depletion of $\delta^{18}O_p$ is also observed going inland (continental effect) and with increased precipitation intensity over the low latitudes (precipitation amount effect). In Fig. 5b, we compare our modeled $\delta^{18}O_p$ with observational dataset. The speleothem pre-industrial values of $\delta^{18}O_c$ in calcite are converted to $\delta^{18}O_p$ in precipitation. The modelled $\delta^{18}O_p$ are in very good agreement with the observations with a linear regression gradient of 0.87 (1.0 being the perfect fit) and a root-mean squared error (RMSE) of 2.3 ‰. This represents an improvement compared to the modeled results from ECHAM5/MPIOM (RMSE of 3 ‰, Werner et al. (2016)). The modelled global $\delta^{18}O_p$ – temperature relationship (for temperature below 20°C, Fig.10c) is also improved with a gradient 0.63 ‰ °C^{-1}(r^2= 0.97), very close of the observed one (0.66 ‰ °C^{-1}, r^2= 0.95). This improvement, compared to the results from Werner et al. (2016), is mainly due to a better model-data agreement for the very low temperatures over the poles, which constitute an extreme test for isotope-enabled GCMs. This is confirmed by the good agreement of our modeled $\delta^{18}O_p$–temperature spatial gradient over Antarctica (0.71 ‰ °C^{-1}, r^2= 0.97) with the gradient of 0.8 ‰ °C^{-1} deduced from the Antarctic isotopic observations compiled by Masson-Delmotte et al. (2008). However, even if the warm bias for the coldest temperatures over Antarctica is reduced, the modeled $\delta^{18}O_p$ values are still too enriched at these locations (Fig. 10b). Concerning the $\delta^{18}O_p$–precipitation spatial gradient, we calculate observed and modeled values of−0.47 and −0.36‰.mm^{-1}.day, respectively, for the 9 low-latitude GNIP stations with an annual mean temperature equal or above 20°C. These results have to be taken with caution because of the few available tropical GNIP station records. The rather large standard errors of the gradients, estimated by using the variance-covariance matrix between the regression coefficients, illustrate well this point (0.165 and 0.145 ‰ mm^{-1} day for GNIP and MPI-ESM-wiso results, respectively).

Simulated results under mid-Holocene conditions are in agreement with the isotopic measurements from ice cores and continental speleothems. MPI-ESM-wiso simulates a depletion in isotopic composition of precipitation from North Africa to the Tibetan plateau via India due to the enhanced monsoons during mid-Holocene. Tropical isotope variations are found to be linked to changes in precipitation rate (amount effect). Both modelled changes in temperature and precipitation rate during the mid-Holocene compared to the pre-industrial period with ECHAM6-wiso are consistent with previous PMIP results, with a warmer northern hemisphere summer and enhanced African and Indian monsoons.

Northern and Southern Hemisphere Monsoons responses to mid-Holocene orbital forcing and global warming rcp8.5 scenario

Northern and Southern Hemisphere Monsoons have been investigated in a multi-model ensemble simulations from PMIP3 and CMIP5 in mid-Holocene and rcp8.5 experiments.

In the Northern Hemisphere both climates exhibit high-latitudes warming and enhanced inter-hemispheric thermal contrast in boreal summer, with an implied strengthening and widening of monsoons. However, changes in the spatial extent and rainfall intensity in future climate are smaller than in mid-Holocene for all Northern Hemisphere monsoons except the Indian monsoon. A decomposition of the moisture budget in thermodynamic and dynamic contributions can help to better address mechanisms responsible for such differences in these two climates. Under future global warming the weaker response of the African, Indian and North American monsoons results from a compensation between both components. On the other hand, the dynamic component, primarily constrained by changes in net energy input over land, determines instead most of the mid-Holocene land monsoonal rainfall response.

In the Southern Hemisphere however, mid-Holocene and rcp8.5 show a contrasting monsoon response. Monsoon weakens and contracts in mid-Holocene as a result of negative net energy input dominating the dynamic component at both global and regional scale. In contrast, SH monsoons strengthen under rcp8.5 as a result of positive net energy input. However the magnitude of positive net energy input is weak, due to compensation effects between the dynamic and thermodynamic components, as shown already in the Northern Hemisphere boreal summer. We find that the degree of compensation between these two components and hence the overall monsoon response is uncertain in rcp8.5 mainly due to the strong intermodel spread in the dynamic term. This stronger local effect is in stark contrast to the Northern hemisphere where the dynamical component of the changes in the moisture budget is more dominant across the model ensemble.

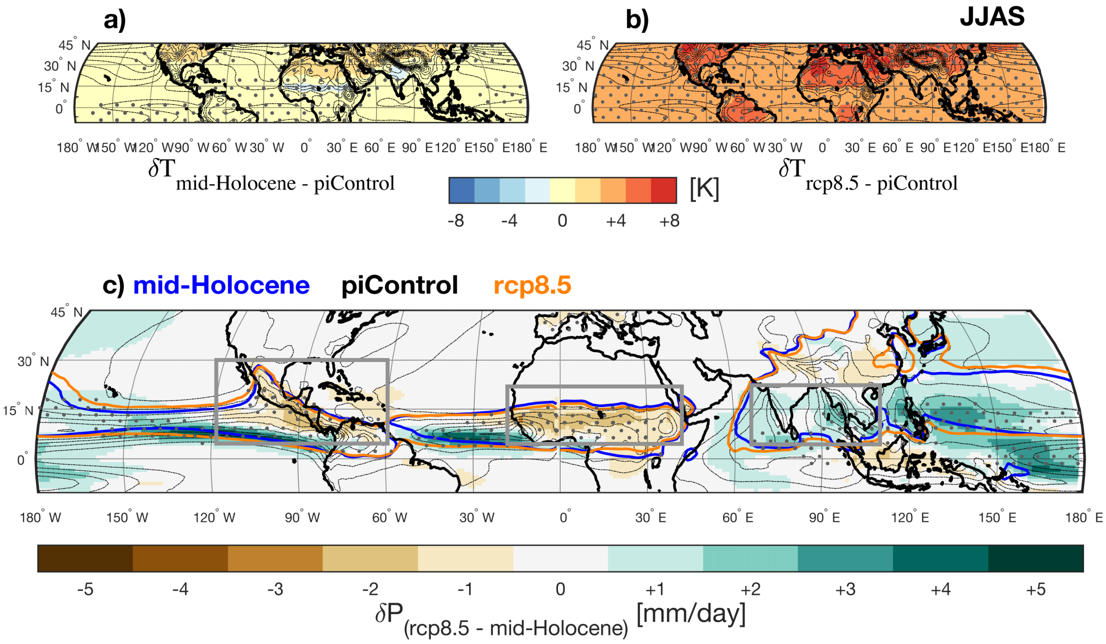

Fig. 6: Surface temperature difference between mid-Holocene (a) and rcp8.5 (b) and piControl in June-to-September (JJAS) ensemble means (shading). Precipitation difference between rcp8.5 and mid-Holocene JJAS ensemble means (c, shading). Black dashed lines in every panel show the piControl as reference (contour interval 2 K for temperature and 2 mm/day for precipitation). Orange and blue bold lines in c) show areas within which the annual precipitation range (JJAS minus DJFM) exceeds 2 mm/day for rcp8.5 and mid-Holocene, respectively. Grey boxes indicate the North American, African and Indian monsoon domains. Stippling indicates areas where at least 8 out of 9 models agree on the sign of the change.

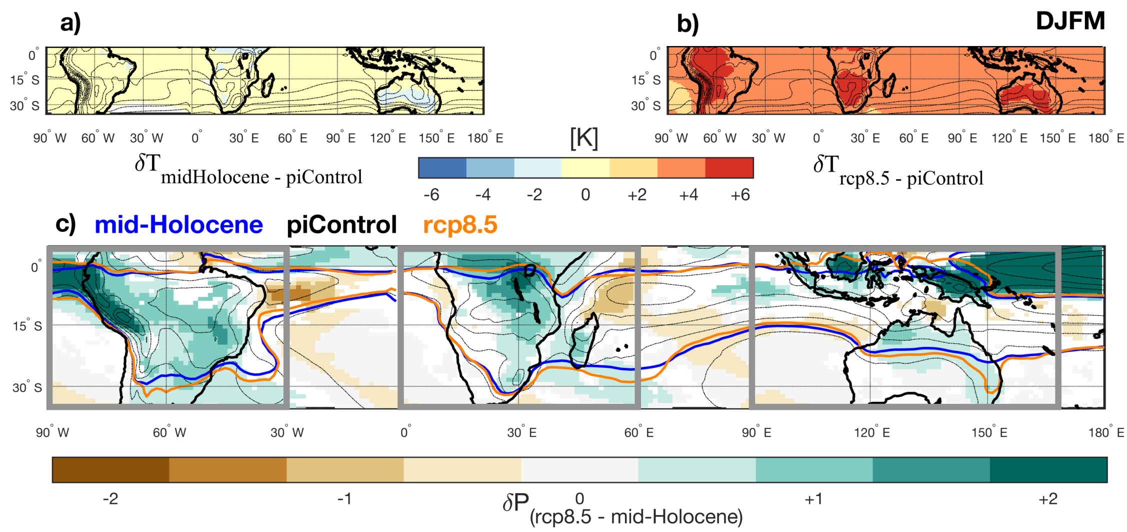

Fig. 7: Surface temperature difference between mid-Holocene (a) and rcp8.5 (b) and piControl in December-to-March (DJFM) ensemble means (shading). Precipitation difference between rcp8.5 and mid-Holocene for DJFM ensemble means (c, shading). Black dashed lines in every panel show the piControl as reference (contour interval 2 K for temperature and 2 mm/day for precipitation). Orange and blue bold lines in c) show areas within which the annual precipitation range (DJFM minus JJAS) exceeds 2 mm/day for rcp8.5 and mid-Holocene, respectively. Grey boxes indicate the South American, South African and Australian monsoon domains. Only areas where two-thirds of models agree on the sign of the change are shown.

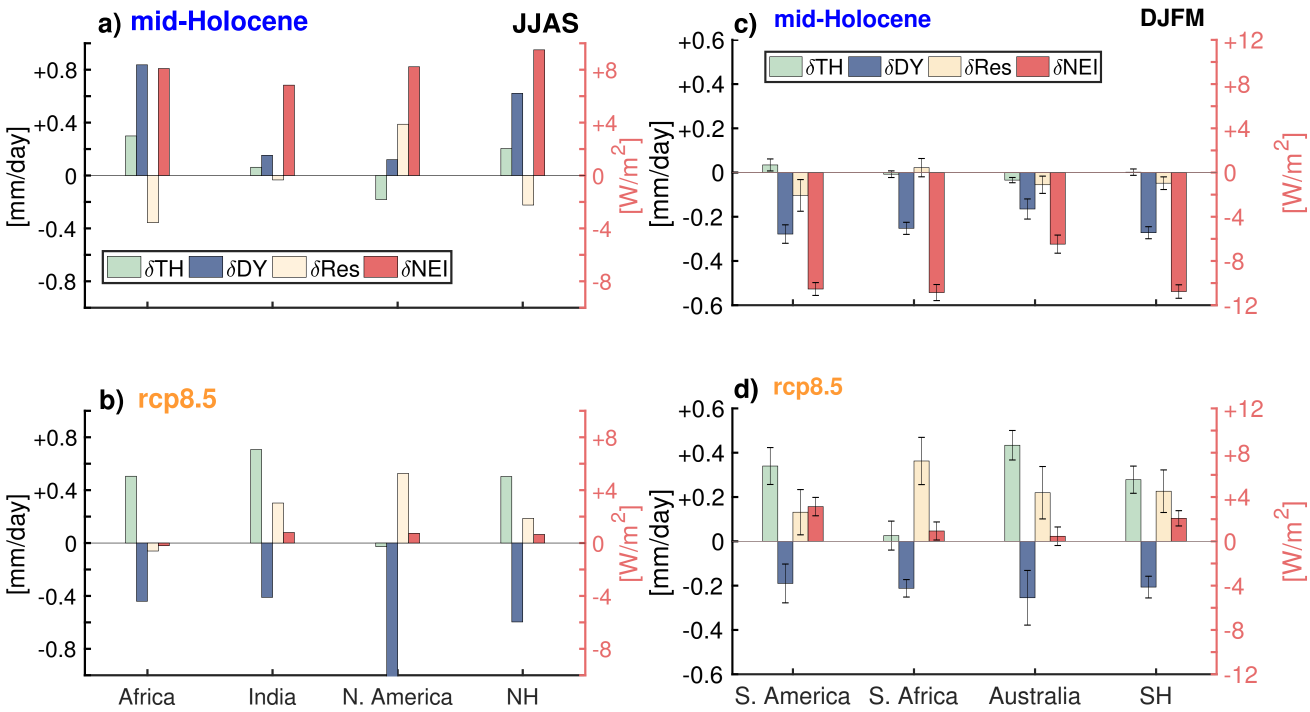

Fig. 8: JJAS and DJFM regionally averaged Net Energy Input (NEI - red axis) changes and changes in thermodynamic (TH) and dynamic (DY) components of the moisture budget, as well as its residual (Res) for mid-Holocene (a, c) and rcp8.5 (b,d) (black axis) for individual monsoons: Northern Hemisphere monsoons on left and Southern on right panels. Note that 8 out of 9 models agree on the sign of the change. Bar ranges indicate the standard error for each contribution computed among the ensemble members.

Tropical Belt variability

Tropical belt (e.g. the size of the intertropical convergence zone, ITCZ) is projected to narrow with global warming (Byrne and Schneider, 2016) because changes in the moist static energy budget. In fact, while MSE advection by the mean circulation and MSE divergence by transient eddies tend to narrow the ITCZ, increase in net energy input and gross moist stability tend to widen it. MPI-ESM transient simulation from mid-to-late Holocene offers the chance to investigate such changes on long time scale, and possibly relate tropical belt variability with monsoon dynamics at regional scale. In fact, while the position of the ITCZ does not change substantially in mid-Holocene than in pre-Industrial simulations, a change in the size of the ITCZ must be expected in order to sustain the monsoon area increase in Northern Hemisphere mid-Holocene summer. In the study we investigate changes in tropical belt over last 8000 years, and its relationship with monsoon dynamics. The size of the tropical belt depends on the mean meridional circulation (e.g. the Hadley circulation) and it is defined here as the size of its ascending branch. (Fig. 9). Figure 9 shows that change in the width of the tropical belt depends mainly on change in the shape of the Northern Hemisphere Hadley cell throughout the simulation. Such circulation responds in fact strongly to change in the net energy input and change in the gross moist stability, impacting therefore the size of the precipitation belt.

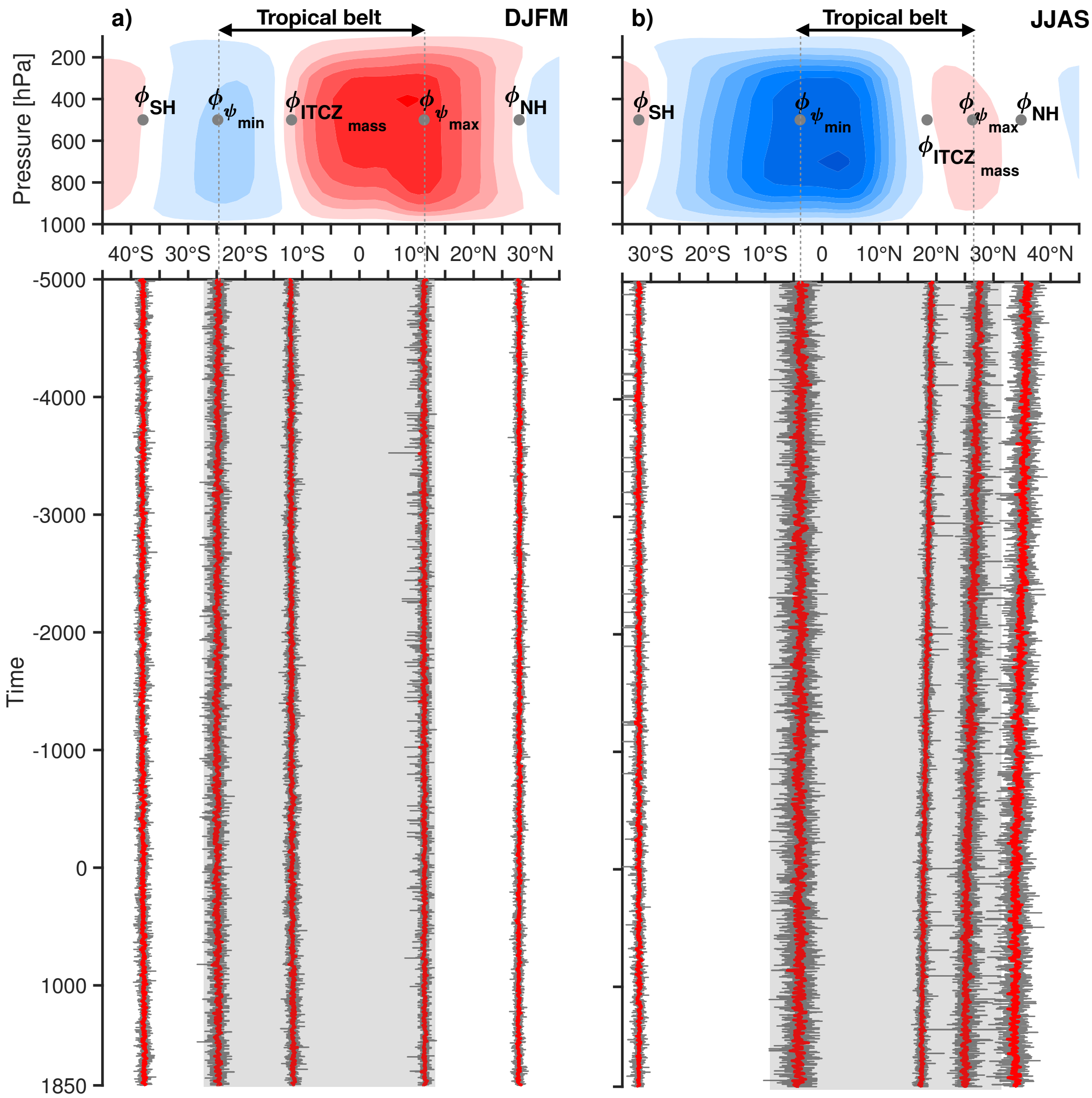

Figure 9: December-to-March (DJFM, a) and June-to-September (JJAS, b) meridional mass stream function (ψ) for MPI-ESM mid-to-late Holocene transient simulations. Upper panels show the mean seasonal ψ for the full length of the simulation. Dots represent the latitude of Hadley cell edges in the Southern and Northern Hemispheres (φSH and φNH, respectively) and the latitude of the mass-ITCZ (φITCZ). The tropical belt lie between the latitude of the minimum (φ ψmin) and maximum (φ ψmax) of Southern and Northern Hadley cell. Lower panels show time series for each of these points (grey lines). 10-years moving averages are shown in red.

D'Agostino, R., Brown, J. R., Moise, A., Nguyen, H., Silva Dias, P. L., Jungclaus, J.: (2019) “Contrasting Southern Hemisphere monsoon response: mid-Holocene orbital forcing versus future greenhouse-gas induced global warming.” *Submitted to Journal of Climate*
D'Agostino, R, Bader, J., Bordoni S., Ferreira, D., Jungclaus J.: (2019) “Northern Hemisphere Monsoon Response to Mid−Holocene Orbital Forcing and Greenhouse Gas−Induced Global Warming.” *Geophysical Research Letters* 46.3: 1591-1601.
Shi, X., & Lohmann, G., 2016, Simulated response of the mid-Holocene Atlantic meridional overturning circulation in ECHAM6-FESOM/MPIOM. Journal of Geophysical Research: Oceans, 121(8), 6444-6469.
Sjolte, J., Sturm, C., Adolphi, F., Vinther, B. M., Werner, M., Lohmann, G., and Muscheler, R.: Solar and volcanic forcing of North Atlantic climate inferred from a process-based reconstruction. Clim. Past, 14, 1179-1194, 2018. doi:10.5194/cp-14-1179-2018
Shi, X., and G. Lohmann, 2017: Sensitivity of open-water ice growth and ice concentration evolution in a coupled atmosphere-ocean-sea ice model. Dynamics of Atmospheres and Oceans 79, 10-30. doi:10.1016/j.dynatmoce.2017.05.003
Gierz, P., M. Werner, G. Lohmann, 2017: Simulating Climate and Stable Water Isotopes during the Last Interglacial using a Coupled Climate-Isotope Model. Journal of Advances in Modeling Earth Systems, 9(5), 2027-2045. doi: 10.1002/2017MS001056
Cauquoin, Alexandre, Martin Werner, and Gerrit Lohmann. "Water isotopes–climate relationships for the mid-Holocene and pre-industrial period simulated with an isotope-enabled version of MPI-ESM.", Climate of the Past, in press
Shi, X., Lohmann, G., Sidorenko, D., and Yang, H.Early-Holocene simulations using different forcings and resolutions in AWI-ESM, submitted to the Holocene
Shi, X., & Lohmann, G., The Northern Hemisphere synoptic processes under early-Holocene regimes, submitted to JGR-atmosphere

References:

Byrne, M. P., & Schneider, T. (2016). Narrowing of the ITCZ in a warming climate: Physical mechanisms. *Geophysical Research Letters*, *43*(21), 11-350.
Egerer, S., Claussen, M., Reick, C., & Stanelle, T. (2015). Marine sediment records as indicator for the changes in Holocene Saharan landscape: simulating the dust cycle. Climate of the Past Discussions, 11(6), 5269-5306.
D'Agostino, R., et al. "Northern Hemisphere Monsoon Response to Mid−Holocene Orbital Forcing and Greenhouse Gas−Induced Global Warming." *Geophysical Research Letters* 46.3 (2019): 1591-1601.
Kinne, S., O'Donnel, D., Stier, P., Kloster, S., Zhang, K., Schmidt, H., ... & Stevens, B. (2013). MAC−v1: A new global aerosol climatology for climate studies. Journal of Advances in Modeling Earth Systems, 5(4), 704-740.
Masson-Delmotte, V., Hou, S., Ekaykin, A., Jouzel, J., Aristarain, A., Bernardo, R. T., Bromwhich, D., Cattani, O., Delmotte, M., Falourd, S., Frezzotti, M., Gallée, H., Genoni, L., Isaksson, E., Landais, A., Helsen, M., Hoffmann, G., Lopez, J., Morgan, V., Motoyama, H., Noone, D., Oerter, H., Petit, J. R., Royer, A., Uemura, R., Schmidt, G. A., Schlosser, E., Simões, J. C., Steig, E., Stenni, B., Stievenard, M., van den Broeke, M., van de Wal, R., van de Berg, W.-J., Vimeux, F., , and White, J. W. C.: A review of Antarctic surface snow isotopic composition: observations, atmospheric circulation and isotopic modelling, J. Climate, 21, 3359–3387, https://doi.org/10.1175/2007JCLI2139.1, 2008.

Nguyen, H., Hendon, H. H., Lim, E. P., Boschat, G., Maloney, E., & Timbal, B. (2018). Variability of the extent of the Hadley circulation in the southern hemisphere: a regional perspective. Climate Dynamics, 50(1-2), 129-142

Nolan, D. S., Zhang, C., & Chen, S. H. (2007). Dynamics of the shallow meridional circulation around intertropical convergence zones. Journal of the atmospheric sciences, 64(7), 2262-2285.

Werner, M., Haese, B., Xu, X., Zhang, X., Butzin, M., and Lohmann, G.: Glacial–interglacial changes in $H_2^{18}O$, HDO and deuterium excess– results from the fully coupled ECHAM5/MPI-OM Earth system model, Geosci. Model Dev., 9, 647–670, https://doi.org/10.5194/gmd-9-647-2016, 2016.